



HAL
open science

Effect of Diffusion Length in Modeling of Equiaxed Dendritic Solidification under Buoyancy Flow in a Configuration of Hebditch–Hunt Experiment

Tao Wang, Sergey Semenov, Engang Wang, Yves Delannoy, Yves Fautrelle,
Olga Budenkova

► **To cite this version:**

Tao Wang, Sergey Semenov, Engang Wang, Yves Delannoy, Yves Fautrelle, et al.. Effect of Diffusion Length in Modeling of Equiaxed Dendritic Solidification under Buoyancy Flow in a Configuration of Hebditch–Hunt Experiment. Metallurgical and Materials Transactions B, 2019, 50 (6), pp.3039-3054. 10.1007/s11663-019-01703-z . hal-02395330

HAL Id: hal-02395330

<https://hal.science/hal-02395330>

Submitted on 20 Nov 2020

HAL is a multi-disciplinary open access archive for the deposit and dissemination of scientific research documents, whether they are published or not. The documents may come from teaching and research institutions in France or abroad, or from public or private research centers.

L'archive ouverte pluridisciplinaire **HAL**, est destinée au dépôt et à la diffusion de documents scientifiques de niveau recherche, publiés ou non, émanant des établissements d'enseignement et de recherche français ou étrangers, des laboratoires publics ou privés.

1 **Effect of Diffusion Length in Modeling of Equiaxed Dendritic**
2 **Solidification under Buoyancy Flow in a Configuration of**
3 **Hebditch-Hunt Experiment**

4 TAO WANG^{1,2,3}, SERGEY SEMENOV², ENGANG WANG^{1,3}, YVES DELANNOY², YVES
5 FAUTRELLE², and OLGA BUDENKOVA²

6 1) Key Laboratory of Electromagnetic Processing of Materials (Ministry of Education),
7 Northeastern University, No. 3-11, Wenhua Road, Shenyang 110004, P. R. China

8 2) Univ. Grenoble Alpes, CNRS, Grenoble INP, SIMAP, F-38000 Grenoble, France.

9 3) School of Metallurgy, Northeastern University, Shenyang 110004, P. R. China

10 Author's email address:

11 TAO WANG: epw_wangtao@163.com

12 SERGEY SEMENOV: s.semionov_1266@mail.ru

13 ENGANG WANG: egwang@mail.neu.edu.cn

14 YVES DELANNOY: yves.delannoy@simap.grenoble-inp.fr

15 YVES FAUTRELLE: Yves.Fautrelle@simap.grenoble-inp.fr

16 OLGA BUDENKOVA: olga.budenkova@simap.grenoble-inp.fr

17 Correspondent: egwang@mail.neu.edu.cn (ENGANG WANG)

T. Wang, S. Semenov, E. Wang, Y. Delannoy, Y. Fautrelle, O. Budenkova, *Effect of Diffusion Length in Modeling of Equiaxed Dendritic Solidification under Buoyancy Flow in a Configuration of Hebditch–Hunt Experiment*, **Metallurgical and Materials Transactions B**, 2019, 50 (6), 3039-3054

Version submitted after revision

18 **ABSTRACT:** Modeling of equiaxed solidification is vital for understanding the solidification
19 process of metallic alloys. In this work, an extended literature review is given for the models
20 currently used for equiaxed solidification simulations. Based on this analysis, we present a
21 three-phase multiscale equiaxed solidification model in which some approximations regarding
22 solute transport at microscopic scale are put together in a new way and incorporated into
23 macroscopic transport equations. For the latter, a term relating to the momentum exchange
24 between the two phases is revised, and a modification for the grain packing algorithm is proposed.
25 A modernized model for equiaxed dendrite growth is tested using a case of solidification of
26 Sn-5wt.%Pb alloy in a parallelepiped cavity that mimics the Hebditch-Hunt experiment. The
27 results obtained using two approaches to calculate diffusion length are presented and compared
28 both with each other and with numerical results from elsewhere. It is demonstrated that diffusion
29 length has a crucial effect on the final segregation pattern.

30

31 **KEY WORDS:** Equiaxed solidification, Macrosegregation, Diffusion length, Grain growth,
32 Multiphase flow

33 I. Introduction

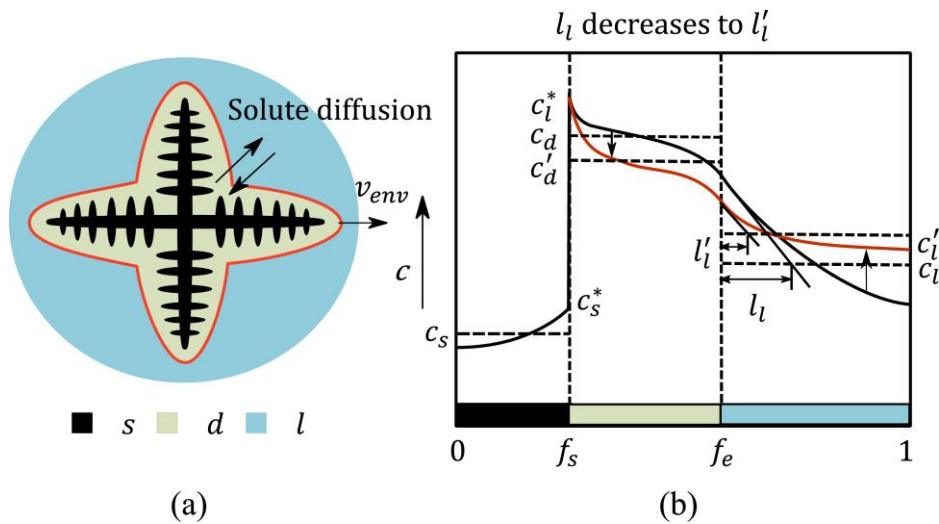
34 Modeling the equiaxed regime for alloy solidification is essential for predicting the structure
35 and composition of solidifying material in the casting process. Indeed, sedimentation or flotation
36 of free equiaxed grains leads to composition inhomogeneity; growth of equiaxed dendrites can
37 block growth of columnar ones either mechanically or by rejected solute and induces columnar to
38 equiaxed transition (CET).^[1,2] However, **despite serious efforts** to develop dedicated numerical
39 models, **such simulation** remains challenging due to the complexity of coupled multiscale
40 phenomena. Indeed, numerical analysis of equiaxed dendritic solidification accompanied by
41 convective flow basically needs to address the following issues: (1) individual grain growth inside
42 an undercooled melt, which is governed by the mass, heat and chemical species transfers **between**
43 **phases**, which, in turn, are affected by grain growth; (2) motion of liquid and growing grains, and
44 corresponding transport of solute concentration, energy and grain number density. Contemporary
45 numerical models propose different approaches to resolve these issues. To provide readers with a
46 clear vision of the differences between the models, an extended review regarding treatment of the
47 aforementioned issues is given in the introduction. **Based on this analysis, in section II we present**
48 **a three-phase multiscale equiaxed solidification model in which some approximations regarding**
49 **microscopic scale phenomena are put together and incorporated into macroscopic mass,**
50 **momentum, energy and solute transportation equations in a new way. Particular attention is paid to**
51 **calculation of diffusion length around the dendrite envelope**, which is crucial for grain growth
52 kinetics. Furthermore, the choice of momentum exchange coefficient, the improvements to the
53 grain packing method, and a double time step algorithm are also explained in detail. The proposed
54 model is applied to simulation of the Hebditch-Hunt experiment, which is briefly described **in**
55 **section III. In section IV**, the results obtained using two approaches to calculate diffusion length
56 are presented and show us the drastic influence of the diffusion length model on the final
57 segregation pattern. These results are also compared with numerical results **that can be found**
58 elsewhere.

59 A. Models for growth of an individual grain *accounting for convection*

60 Regarding diffusive growth of an individual dendrite grain, most models are based on the
61 utilization of three phases as was initially proposed by Thévoz et al.^[3]. These three phases (see
62 Figure 1) are: the solid dendrite, or *s*-phase; the liquid between the solid dendrite arms, the

63 so-called interdendritic liquid, or d -phase; and the liquid outside of the dendrite envelope, the
 64 so-called extradendritic liquid, or l -phase. Each phase is characterized by a corresponding volume
 65 fraction and averaged values for velocity, temperature and solute concentration. The liquid
 66 concentration at the solid-liquid interface c_i^* is generally supposed to be equal to the
 67 thermodynamic equilibrium concentration, which is related to local temperature through a phase
 68 diagram. In most three-phase models, the interdendritic liquid is considered well mixed, and its
 69 average solute concentration c_d is equal to $c_i^{*[4-7]}$. Alternatively, for example in a model by Wu
 70 et al.^[8], the value of c_d is calculated according to the diffusion rate at both s - d and l - d interfaces,
 71 as shown schematically in Figure 1(b). This approach maintains a small gap between c_d and c_i^* ,
 72 avoiding the fluctuation of solute concentration in case of abrupt change in temperature, and thus
 73 enhancing model stability under convective flow.

74



75

76 Fig. 1—(a) Schematic representation of grain growth with phase assignment, and (b) effect of
 77 diffusion length on average solute concentration in each phase.

78 The transition from the liquid to the solid phase can be seen as a combination of dendrite growth,
 79 associated with the elongation of the primary dendrite arms at the expense of the extradendritic
 80 liquid, and the lateral growth of secondary arms during which the interdendritic liquid solidifies.

81 In theory, dendrite tip growth velocity can be calculated accounting for the convective flow that
 82 leads to cumbersome expressions.^[9,10] Therefore, in macroscopic models, it is generally accepted
 83 that dendrite tip growth velocity can be estimated using the Lipton-Glicksman-Kurz (LGK)
 84 model^[11] in steady diffusive growth, or using modified LGK models^[12,13] when accounting for

85 **convection.** In the LGK model, tip growth velocity v_{tip} depends on the constitutional
 86 undercooling ahead of the dendrite tip or ahead of a so-called grain envelope. This undercooling
 87 corresponds to the local difference between c_l^* and external liquid concentration c_l . According to
 88 the scheme presented in Figure 1, this difference greatly depends on the diffusion length in l -phase
 89 denoted by l_l . A theoretical solution for l_l exists for diffusive growth of a single grain under
 90 steady conditions^[14] that gives:

$$l_l = \frac{D_l}{v_{tip}} \quad [1]$$

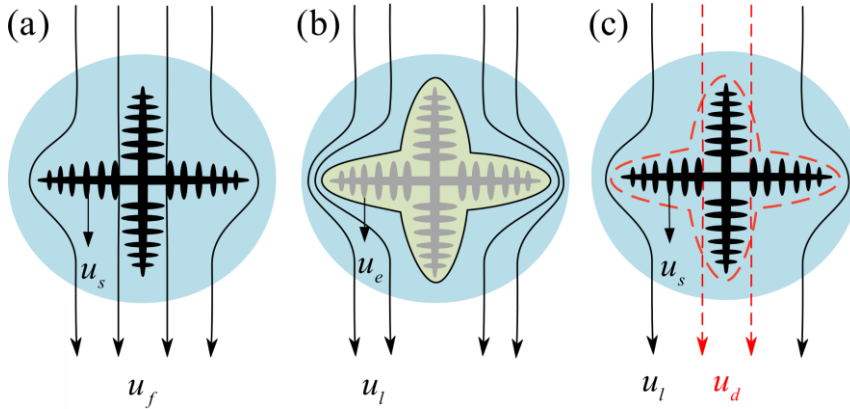
91 where D_l is the solute diffusion coefficient in l -phase, and v_{tip} is the primary dendrite tip
 92 velocity. For a spherical envelope, v_{tip} is also the l - d interface movement velocity relative to
 93 grain growth. For a non-spherical envelope, v_{tip} should be replaced by $v_{env} = \phi_M v_{tip}$, ϕ_M is a
 94 shape factor.

95 This formulation was used by Wu et al.^[8] in the equiaxed solidification problem with grain
 96 transportation and fluid flow **although it does not take into account** the intensification of the
 97 diffusive flux by convection. It can be assumed that convection leads to a smaller diffusion length
 98 than that defined by Eq. [1], i.e. transport of the solute from the d -phase to the l -phase will be
 99 intensified, thus promoting enrichment of the l -phase. **To take this into account, for example, in a**
 100 **three-phase model by Wang et al.,^[13] a relative velocity between the l - and the s - phases was**
 101 **introduced in the expression for l_l . For two-phase models, which can be globular^[15-17] or**
 102 **dendritic,^[18] there is no distinction between d - and l -phases: instead, a liquid phase, or f -phase, is**
 103 **considered. In this case, the diffusion length in the f -phase is denoted by l_f . In the two-phase**
 104 **model by Ni et al.,^[17] the effect of convective flow was accounted for via a Sherwood number,**
 105 **which had to be, however, carefully chosen from experimental data.^[19] According to Wang et al.,^[7]**
 106 **in a dendritic growth of equiaxed grains with spherical envelope shape, diffusion length l_l should**
 107 **be smaller than the value given by Eq.[1] to keep a continuous enrichment process of the l -phase.**
 108 **A similar criterion was used in a non-spherical equiaxed solidification model by replacing tip**
 109 **velocity with an envelope growth velocity.^[8] To satisfy this, in the description of mass transport**
 110 **for a single equiaxed crystal moving in an infinite medium, Appolaire et al.^[12] used a boundary**
 111 **layer around an equivalent sphere accounting for the convection as l_l and then limited its**
 112 **maximum value by the length given in Eq. [1]. The most representative models for diffusion**
 113 **length are grouped in Table I.**

114

115 B. Motion of liquid and dendrites: “hydrodynamic” phases, drag force

116 The expression of the momentum exchange or drag force between phases i and j , denoted as
 117 \vec{U}_{ij}^D , depends on the choice of phases that represent macroscopic motion in the system. The phase j
 118 related to the dendritic grain can be presented **only as the solid dendrite in the liquid (Figure 2(a)),**
 119 **or as a union of the solid dendrite and the interdendritic liquid (grain) in the extradendritic liquid**
 120 **(Figure 2(b)). In the latter case, however, a difference in macroscopic velocities between the solid**
 121 **phase, inter- and extradendritic liquid can be taken into account $\vec{u}_d \neq \vec{u}_l$ (Figure 2(c)).**



122

123 Fig. 2—Schematic figure for different unions of phases: (a) solid dendrite (s - phase) and liquid
 124 phase (f -phase), (b) equiaxed grain phase (e -phase) and extradendritic liquid phase (l - phase), and
 125 (c) the solid dendrite (s -phase), inter- and extradendritic liquid phases (d - and l -phases).

126 In an averaged description, the phase j that represents dendrites is generally considered to be a
 127 porous medium, due to the complexity of an individual dendrite structure. It is customary to treat
 128 the momentum exchange while the liquid phase i is passing through a medium phase j using a
 129 generalized exchange coefficient K_{ij} and the difference in phase velocities. K_{ij} can be expressed
 130 either via a configuration factor $F_K(f_j, d_j)$ and permeability K of the solidifying phase, or via
 131 another configuration factor $F_{CD}(f_j, d_j)$ along with a notion of a drag coefficient C_D , resulting
 132 from consideration of a particle moving through the liquid:

$$\vec{U}_{ij}^D = K_{ij}(\vec{u}_i - \vec{u}_j) = F_K(f_j, d_j) \frac{\mu_i}{K} (\vec{u}_i - \vec{u}_j) = F_{CD}(f_j, d_j) C_D \rho_l |\vec{u}_i - \vec{u}_j| (\vec{u}_i - \vec{u}_j) \quad [2]$$

133 In Eq. [2] both functions $F_K(f_j, d_j)$ and $F_{CD}(f_j, d_j)$ depend on the fraction and characteristic
 134 size and sphericity of the particles of phase j . Note that the drag coefficient C_D can take into
 135 account the permeability of phase j and thus that the two configurations indicated above can be

136 equivalent. Different approximations for these functions and coefficients (see Table II) can be
137 found in literature.

138 The most **common** model, traditionally used for permeability of the mushy zone in columnar
139 dendrite growth, is the Kozeny-Carman relation^[20] (Table II), which was formulated for the
140 pressure drop in a laminar flow passing through a stationary packed column. The latter was treated
141 as a bundle of tangled tubes of various cross-sections. This relation was used in the model with
142 two phases and globular equiaxed grains developed by Wu et al.^[21] and further adopted by these
143 authors for the drag force between *l*-phase and *e*-phase $\vec{U}_{le}^D = -\vec{U}_{el}^D$ (Figure 2(b)) in a three-phase
144 model.^[22]

145 **In another two-phase solidification model with globular equiaxed grains**, Ni et al.^[17] used an
146 expression for the drag coefficient C_D that accounted for a modification of flow character during
147 the solidification process. **For low solid fractions** ($f_s < 0.5$) the grains were supposed to move
148 relatively freely in the liquid, i.e. the interfacial momentum balance between the solid and liquid
149 could be presented using Stokes' law for an individual object moving through the liquid. For
150 $f_s > 0.5$, the solid phase was similar to a packed bed, thus allowing momentum balance to be
151 presented with the Kozeny-Carman expression. A similar approach was adopted by Leriche et al.^[4]
152 in a three-phase model. For slurry regions, they applied the model used by Ni et al.^[17] but replaced
153 the solid-phase fraction with a grain-phase fraction. For packed regions, a permeability related to
154 secondary arm spacing is applied.

155 In Wang et al.'s model,^[13] the *l*- and *d*-phases were united as the *f*- phase: $f_f = f_d + f_l$, yet, the
156 difference between velocities \vec{u}_d and \vec{u}_l was preserved (Figure 2(c)). An expression for the
157 momentum exchange coefficient K_{fs} (Table II) between *f*- and *s*-phases was obtained for all solid
158 fractions ranging from 0 to 1 through a general correlation $K_{fs} = \{[(1 - f_l)K_{ds}]^n + (K_{le})^n\}^{1/n}$. In
159 this equation, coefficient K_{ds} was evaluated **from the secondary dendrite arm spacing, and**
160 coefficient K_{le} was taken from Happel's approach that considered the viscous flow relative to the
161 bed of spherical particles^[23]. Wang et al.'s model^[13] took into account a shape factor $C_p(\Phi_e)$ for
162 the dendrite grain to provide freedom for estimation of surface area concentration.

163 In Appolaire et al.'s work^[12], another model proposed for the momentum exchange coefficient
164 in a three-phase system was verified with the equiaxed grain sedimentation experiment. **Table II**
165 **gives** more details on different models for calculating the momentum exchange coefficient.

166 As indicated above, another important phenomenon related to the motion of equiaxed grains is
167 their packing, after which the grains can be considered immovable. However, for the sake of
168 brevity, in this paper we prefer not to discuss the various models used to implement packing
169 phenomena: some references are indicated elsewhere^[24]. A description of the procedures used in
170 the model is given below in section II-C.

171

172 II. Description of the present model

173 The present model is based on three phases, which consist of the liquid outside of the envelope
174 of equiaxed dendrite (*l*-phase), the interdendritic liquid (*d*-phase), and the solid dendrite (*s*-phase)
175 (Figure 2(b)). The phase fractions satisfy the following constraint: $f_d + f_s + f_l = 1$. A union of the
176 solid dendrite and the interdendrite liquid makes the grain phase $f_d + f_s = f_e$. The solid and grain
177 phase should appear in the volume once nucleation has occurred. Nucleation is assumed to occur
178 instantaneously once local constitutional undercooling is greater than nucleation undercooling
179 $\Delta T > \Delta T_{nucl}$, or if the local grain number density n drops below 1 m^{-3} ^[16]. The latter condition is
180 used to avoid null grain number density that leads to significant numerical errors. During the
181 growth stage, the primary dendrite tip velocity v_{tip} calculated by the LGK model^[11] is multiplied
182 by a shape factor ϕ_M to obtain the envelope growth velocity v_{env} . In this work, the value for
183 ϕ_M is given as 0.683^[22] assuming an octahedral grain envelope shape, although its exact value
184 needs to be measured based on experimental results. Dendritic envelope surface area concentration
185 S_e^M is evaluated based on a spherical envelope shape, as in most works^[6,14,16,25]. Solidification of
186 the interdendritic liquid is governed by solute diffusion in the interdendritic liquid region.
187 Diffusion length inside the interdendritic liquid is assumed to be half of the distance between the
188 secondary dendrite arms (given in Table IV), whereas solid back diffusion is ignored. Regarding
189 the macroscopic multiphase flow, it is assumed that the interdendritic liquid and the solid dendrite
190 share the same velocity field, i.e. the solid phase moves together with some amount of the liquid
191 around it. In the conservation equations, all densities are constant and equal to the reference
192 density, that is $\rho_l = \rho_s = \rho_e = \rho_d = \rho_{ref}$. Similar to Založnik and Combeau,^[16] to model the
193 sedimentation phenomenon, in the buoyancy term, a constant difference between the solid phase
194 density and a reference density is introduced. The Boussinesq approximation accounts for solutal
195 and thermal convection in the liquid phase. While the grain growth model and macroscopic

196 conservation equations are similar to those described elsewhere,^[22] we propose a new combination
 197 of parameters to model the diffusion length between the inter- and extradendritic liquid. Further, a
 198 Happel model is used for implementation of the drag force, and a new grain packing algorithm is
 199 proposed. The reasons for these choices and their crucial effect on the evolution of the
 200 solidification processes are explained in detail below. Conservation equations, source terms, and
 201 some auxiliary expressions, are summarized in Table III, while the main physical parameters are
 202 provided in Table IV.

203 A. Diffusion length model

204 Determination of diffusion length, especially the diffusion length around the envelope in the
 205 extradendritic liquid l_l , drastically affects numerical results as it links phase transition with the
 206 enrichment of the extradendritic liquid. According to Eq. [21] and Figure 1, if l_l decreases, the
 207 solute flux through the envelope intensifies, and the concentration difference between the inter-
 208 and extradendritic liquid decreases if the average concentration is conserved within the volume
 209 corresponding to the final grain size. Consequently, a smaller solutal undercooling ahead of the
 210 dendrite tip leads to a smaller dendrite growth rate (Eq. [34]). This means that the solid fraction
 211 within grain phase f_s^e increases and could promote the sedimentation or floatation of equiaxed
 212 grains. Different methods, proposed for calculation of l_l , are discussed above in the introduction,
 213 and provided in Table I. All of them emphasize several factors, namely dendrite tip velocity,
 214 current and final diameter of the grain (or envelope), and relative velocity between the grain and
 215 the liquid phases. In the present work, the diffusion length proposed by Ni et al.^[17] is adapted for
 216 the three-phase model, and, following the work of Appolaire et al.^[12], we limit its maximum value
 217 by the length given in Eq. [1], replacing v_{tip} by v_{env} since a non-spherical envelope shape is
 218 considered.

$$l_l = \min \left[\frac{d_e}{2} \left(\frac{1}{1 - (1 - f_l)^{\frac{1}{3}}} + \frac{Sc^{\frac{1}{3}} Re^a}{3f_l} \right)^{-1}, \frac{D_l}{v_{env}} \right] \quad [35]$$

219 where $Sc = \mu_l / (\rho D_l)$ is the Schmidt number, $Re = |\vec{u}_l - \vec{u}_e| (\rho f_l d_e) / \mu_l$ is a local Reynolds
 220 number calculated with the envelope diameter d_e , and $a = (2Re^{0.28} + 4.65) / (3Re^{0.28} + 4.65)$.

221 In the first term inside the max operator in Eq. [35], the fraction $1/(1 - (1 - f_l)^{1/3})$ accounts
 222 for the effect of solute interaction, while the term $Sc^{1/3} Re^a / (3f_l)$ describes the effect of
 223 convection around the equiaxed grain envelope. In order to quantitatively illustrate the

224 contribution of each individual physical phenomenon (accounted for in the Eq. [35]) and the
 225 influence of the diffusion length model on phase evolution, a numerical study was conducted for a
 226 zero-dimension solidifying system in which temperature is assumed to be uniform in the
 227 calculation domain and governed by the following equation:^[14] $c_p \dot{T} = L(df_s)/dt - c_p m(dc_l^*)/$
 228 dt . In this case c_p is capacity, L is latent heat, m is the slope of liquidus in the phase diagram,
 229 and $\dot{T} = 1\text{K/s}$ is the imposed cooling rate. Calculations are carried out for the Sn-5wt%Pb alloy,
 230 the same as that investigated in section III, the properties of which are given in Table IV. The total
 231 concentration of the solute in the calculation is conserved.

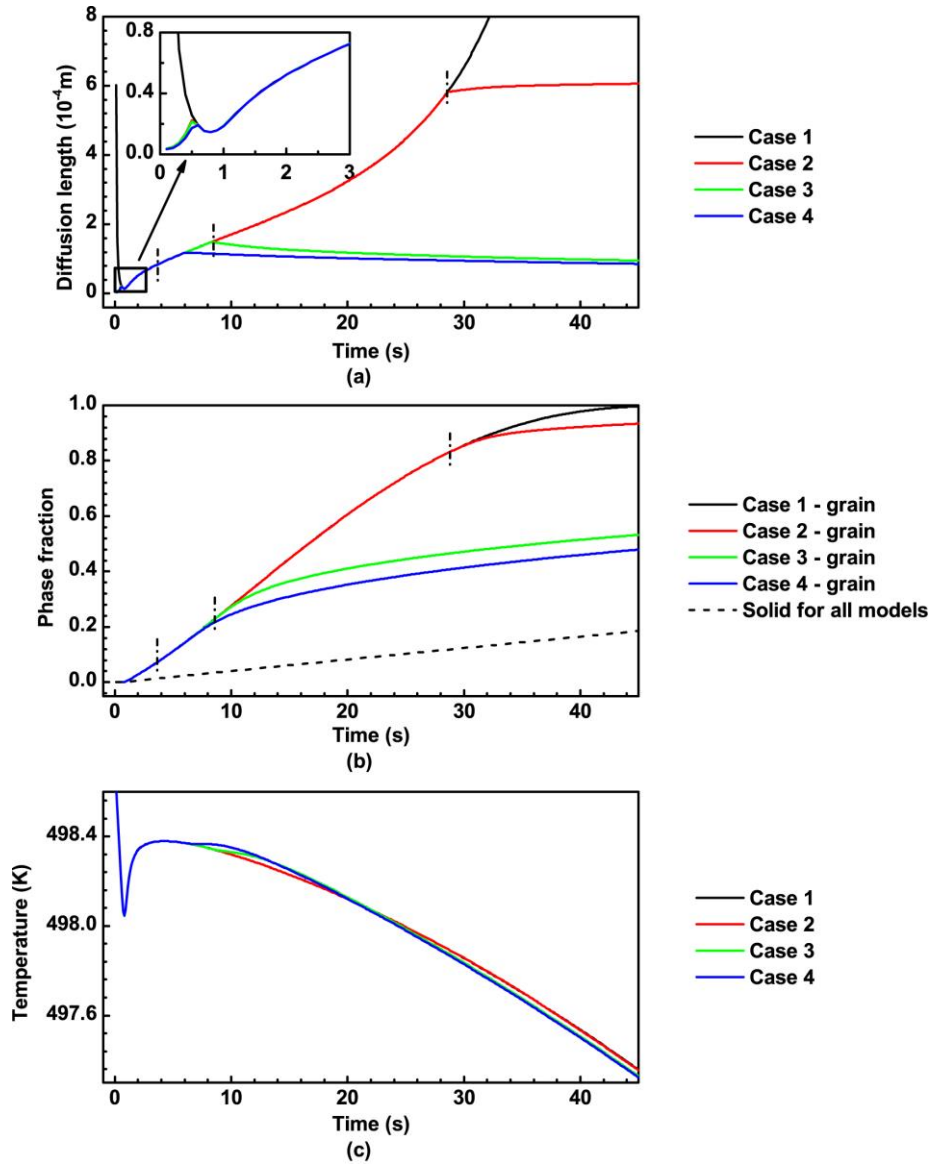
232 Four different diffusion length models are compared: the one given by Eq. [35] and three others
 233 given by Eqs. [36] through [38]:

$$l_l = \frac{D_l}{v_{env}} \quad [36]$$

$$l_l = \min \left[\frac{d_e}{2}, \frac{D_l}{v_{env}} \right] \quad [37]$$

$$l_l = \min \left[\frac{d_e}{2} \left(\frac{1}{1 - (1 - f_l)^{\frac{1}{3}}} \right)^{-1}, \frac{D_l}{v_{env}} \right] \quad [38]$$

234 In case 1, we use a diffusion length that is determined by envelope growth velocity (Eq. [36]).
 235 In case 2, based on Eq. [37], the model assumes that, at the initial growth stage, the thickness of
 236 the diffusion boundary layer around the envelope is comparable with the grain's radius. In case 3
 237 (Eq. [38]), the solute interaction is taken into account, and thus diffusion length can decrease at the
 238 later solidification stage. It should be noted that these phenomena were already taken into
 239 account in the models proposed by Martorano et al.^[26] and Ciobanas et al.^[5] However, their
 240 models are not considered here because they did not deal with convection. Finally, in case 4,
 241 where we use Eq. [35], the convection around envelope is included in the model in addition to the
 242 previously described effects. In order to use Eq. [35], some additional parameters are required.
 243 Grain number density is given a value of $10^9/\text{m}^3$ to determine final grain size. Velocity difference
 244 $|\vec{u}_l - \vec{u}_e|$ is imposed to be 0.1 mm/s, assuming a weak liquid flow around the grains. Results of
 245 simulations are presented in Figure 3.



246
 247 Fig. 3— Solidification in a zero dimension uniformly solidifying system obtained with different
 248 models (Eqs. [35] through [38]) for diffusion length l_i : (a) variation of diffusion length l_i in time,
 249 (b) evolution of the solid and grain fractions and (c) temperature evolution.

250

251 At the early stage ($t < 0.6$ s) of grain growth, grain size is small while the value of D_l/v_{env} is
 252 high. Hence, in the expression of Eqs. [35], [37] and [38], the first term in the bracket prevails,
 253 and case 1 differs from the 3 other cases: see the insert in Figure 3(a). Meanwhile, the effect of
 254 convection and solute interaction is negligible. A second growth stage can be identified during a
 255 time period from 0.6 s to 2.9 s, when v_{env} increases rapidly, and the second expression in Eqs.
 256 [35], [37] and [38] becomes smaller. Consequently, the value of the diffusion length for all 4 cases
 257 is calculated with the same expression, and evolution of phase fractions (Figure 3(b)) and

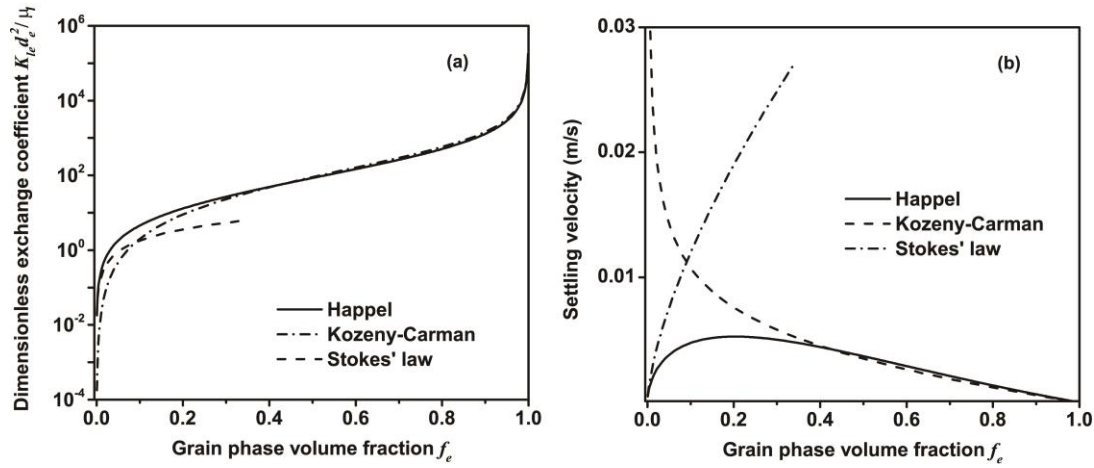
258 temperature (Figure 3(c)) in all four cases is almost equivalent. After 2.9 s, the four cases show
 259 obvious differences. For case 1 and case 2, diffusion length increases in a similar way until
 260 approximately 29 s since v_{env} decreases. In case 3 and case 4, solutal interaction and convective
 261 effect become important. Therefore, although in both Eqs. [35] and [38], the first term in the
 262 brackets is chosen, the diffusion length calculated with Eq. [35] is smaller due to convection, that
 263 also affects the evolution of the grain fraction (Figure 3(b)). It is interesting to note that the
 264 diffusion length evolution observed by Torabi Rad et al.^[27] experienced similar 3 stages as in cases
 265 2 through 4, although that simulation was made for another alloy system and under a different
 266 cooling condition. A remarkable difference in envelope growth is observed between case 1 and
 267 case 4 after 45s of solidification. In the former, the envelopes of neighboring grains impinge
 268 ($f_e \approx 1$), and further solidification occurs in the interdendritic liquid, yet the grain fraction in case
 269 4 is only 0.48. Such a difference can greatly influence the solidification process and
 270 macrosegregation pattern. Regarding the macroscale model, the effect of convective flow on
 271 equiaxed solidification is even more complex since the average solute concentration for a given
 272 grain may also change due to solute or grain transportation at the macroscale. This effect is shown
 273 in section IV.

274

275 B. Momentum exchange coefficient

276 Based on a direct comparison of the non-dimensional momentum exchange coefficients
 277 $K_{le}d_e^2/\mu_l$ calculated with the Happel model^[23] and the Carman-Kozeny model^[20] (Figure 4(a)),
 278 the difference between them could be thought to be minor. Yet, a simple demonstration can be
 279 made with the settling velocity u_e of grains falling in a stationary liquid. This can be calculated
 280 from the equilibrium between the gravitational force and the friction from the liquid as $u_e =$
 281 $\Delta\rho g/K_{le}$. We estimated this velocity for different grain fractions using the grain number density
 282 $n = 10^9 \text{m}^{-3}$ (for calculation of the grain diameter d_e) and the density difference $\Delta\rho =$
 283 100kg/m^3 . Figure 4 (b) presents the results obtained with the two models, while the velocity
 284 calculated with the classical Stokes' drag force is also included for comparison. For a large grain
 285 fraction region, i.e. $f_e > 0.4$, the Happel model and Kozeny-Carman model predict similar
 286 settling velocity, which approaches zero as the amount of liquid decreases. However, for grain
 287 fractions approaching zero, the settling velocity calculated with the Happel model also moves to

288 zero, similarly to the case with the Stokes' law, while use of the Kozeny-Carman equation gives a
 289 velocity value moving to infinity. One can conclude that the Happel model provides a good
 290 approximation both for the free-particle regime, also including very small nuclei, and the packed
 291 bed regime. It should be noted that the model used by Wang et al. ^[13] (Table II) is reduced to the
 292 Happel model if the partition of the inter- and extradendritic liquid phases is not considered.



293

294 Fig. 4—Comparison of (a) dimensionless momentum exchange coefficient between l - and e -
 295 phases and (b) settling velocity between different models.

296

297 C. Grain packing method

298 During solidification, the free-floating equiaxed grains impinge before being packed in a rigid
 299 structure similar to columnar grains. In numerical models, this transition is treated with a packing
 300 fraction limit, which can be associated either with grain fraction f_p^e or with solid fraction f_p^s ,
 301 depending on the phases whose relative motion is considered. Generally, it is assumed that for a
 302 freely moving equiaxed grain, whose volume fraction increases to the packing fraction limit, its
 303 velocity should drop to zero. It is widely accepted that the packing fraction limit for the grain
 304 phase is $f_p^e = 0.637$ ^[4,22,28], which is an approximation of the closest packing fraction of
 305 randomly arranged monodisperse spheres. For solid fraction, the limit is lower and accepted to be
 306 in the range $f_p^s = 0.1 \sim 0.5$, ^[24,29,30]. A more complex morphology of the solid dendrites makes
 307 them easier to form a packed structure. ^[31] A widely used packing condition is that f_e is higher
 308 than f_p^e . However, even if $f_e \geq f_p^e$, grains cannot be made rigid when they are in the middle of a
 309 non-rigid domain, as a group of them could still sediment or float up or be dragged. Thus, in order
 310 to avoid unphysical system behavior, the second packing condition is introduced to the model,

311 which assumes that the grains to be packed should have a rigid neighbor upon which to be
312 attached. A grain packing status marker i_p is adopted to identify whether or not the grains in a
313 calculation cell should be packed. During initialization, a zero value is assigned to i_p in each
314 calculation cell. If the cell of interest is adjacent to the wall or has at least one packed neighboring
315 cell, its i_p value is changed to 1. For the cell marked with $i_p = 1$, once $f_e \geq f_p^e$ is satisfied, the
316 grains get packed and the marker i_p is set to 2, which means that the grain phase motion must be
317 stopped. This procedure is repeated at each time integration step.

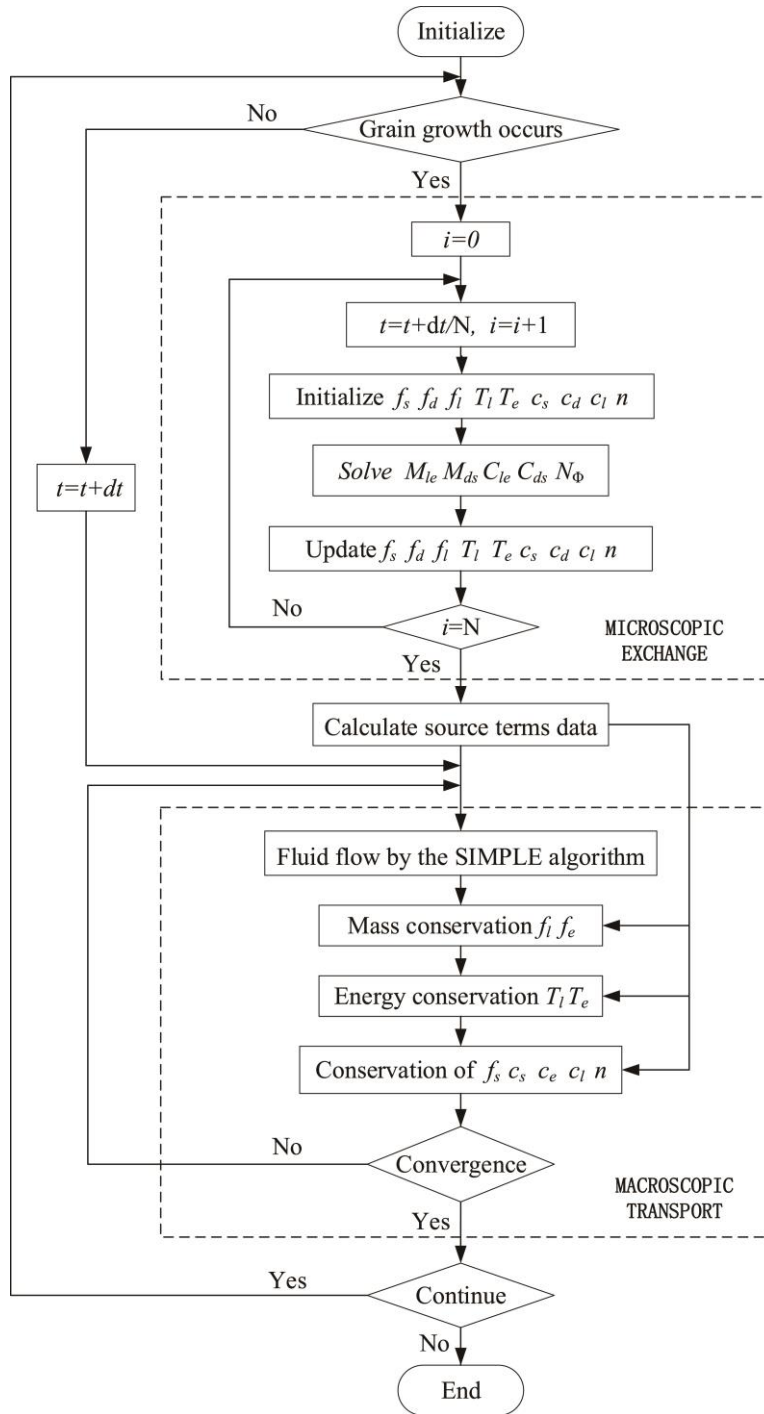
318

319 D. Implementation of the solution algorithm

320 To reduce simulation time, the processes occurring at macroscopic and microscopic scales are
321 modeled with different time step sizes, as shown in Figure 5.

322 For each intensive medium property Ψ , representing phase fraction, solute concentration,
323 temperature or grain number density, a balance equation can generally be written as: $(d(\rho\Psi))/$
324 $d\tau + \nabla(\rho\vec{u}\Psi) = \nabla(\lambda_\Psi\nabla\Psi) + S_\Psi$, where the convection term $\nabla(\rho\vec{u}\Psi)$ and the diffusion term
325 $\nabla(\lambda_\Psi\nabla\Psi)$ represent macroscale transport phenomena. The source term S_Ψ is mainly induced by
326 microscale evolution, including the nucleation and exchange of mass, energy and solute between
327 phases. A double time step method is based on an assumption that microscopic exchange only has
328 a slight influence on macroscopic transportation. A larger time step size Δt , used for calculation
329 of macroscopic transportation, is divided into N sub-steps $\Delta\tau = \Delta t/N$ used for time integration
330 of the microscopic exchange rate.

331 Microscopic exchange is calculated locally by omitting the macroscale transport terms giving
332 $(d(\rho\Psi))/d\tau = S_\Psi$. Each variable is initialized as Ψ_0 , which is the transport solution from the last
333 time step. The value at sub-step i is calculated with the first-order time integration scheme using
334 data from the previous sub-step $i-1$: $\rho\Psi_i = \rho\Psi_{i-1} + S_{\Psi,i-1}\Delta\tau$. In each sub-step, at first an amount
335 of nuclei $(N_\Phi\Delta\tau)/N$ is added, then the rate of phase transition is determined, after that, the solute
336 concentration and enthalpy content are calculated for each phase. Finally, the values of
337 $\sum_{i=1}^N S_{\Psi,i} = \rho(\Psi_N - \Psi_0)/\Delta t$ are recorded and then used as source terms for solving macroscopic
338 transport equations, including multiphase flow field and transport of energy and solute
339 concentration. These macroscopic transport equations are solved by ANSYS FLUENT® software.
340 In current research, we use the time step size Δt of 0.005s and the number of sub-steps N of 20.



341

342 **Fig. 5—Solution algorithm scheme.**

343

344 III. Description of the simulated case

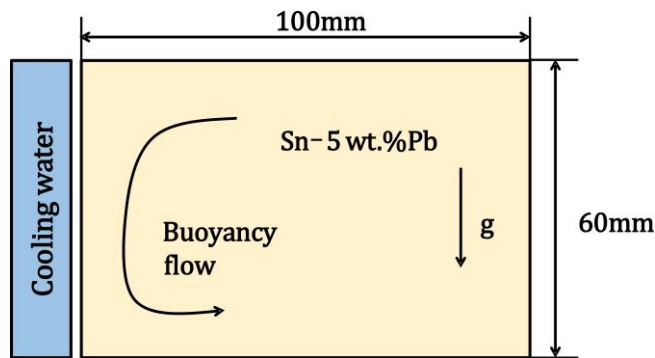
345 The numerical model described above is applied to solidification of a binary alloy, which occurs

346 in a quasi-two-dimensional thin parallelepiped cavity with dimensions 100mm width ×

347 60mm height. Initially, the melt inside the cavity is kept at a uniform temperature slightly above its

348 liquidus temperature. One of the lateral faces of the cavity is then cooled down while other faces are

349 kept adiabatic (Figure 6). This solidification process mimics an experiment performed for the first
 350 time by Hebditch and Hunt^[32] for three binary alloys, one of which was Sn-5wt%Pb, to study the
 351 effect of buoyancy convection on macrosegregation. Since then the experiment has been modeled
 352 many times using models for columnar solidification^[33,34] as well as models that included motion of
 353 the equiaxed grain phase^[35,36]. In our simulation, the initial temperature of the melt is 499.15K,
 354 with a small superheat of about 0.43K above the liquidus temperature of the alloy. The outside
 355 temperature and heat transfer coefficient at the cooling face are 298.15K and $300\text{W m}^{-2}\text{s}^{-1}$,
 356 respectively. All thermophysical parameters and material properties are listed in Table IV, most of
 357 which are taken from the work^[36].



358
 359 Fig. 6—Illustration for the solidification problem under consideration.

360

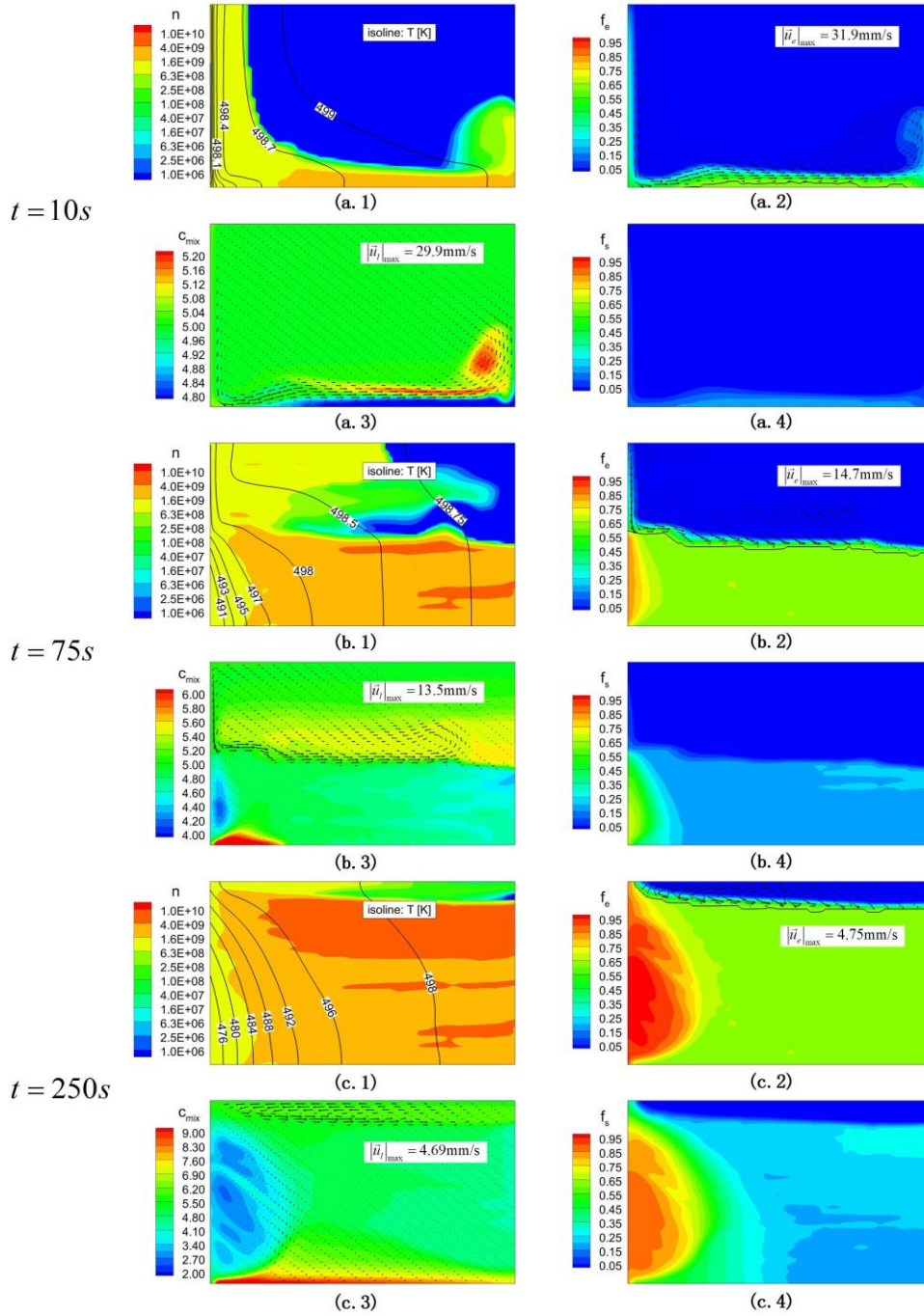
361 IV. Results and discussion

362 For convenience, the simulation performed with diffusion length given by Eq. [35] and
 363 presented in this section IV.A is referred to hereafter as case A. To demonstrate the crucial effect of
 364 diffusion length on the resulting solidification pattern, a simulation presented in section IV.B and
 365 referred to as case B, is performed with the diffusion length given by Eq. [36]. Other internal
 366 parameters, material properties, and external conditions for cases A and B are identical.

367 A. Results of case A

368 At the beginning of the solidification process, the liquid next to the cooling side flows
 369 downwards due to the thermal and solutal buoyancy effects. Nucleation occurs once local
 370 undercooling is greater than nucleation undercooling. According to material properties (see Table
 371 IV), the solute-poor grains have higher mass density than liquid. Therefore, subjected to drag force
 372 and gravity, they are further transported by the fluid flow, sediment, and accumulate at the cavity
 373 bottom. In solidification, the partition coefficient for Pb is less than one, meaning that the solid
 374 initially forms at a depleted composition relative to the nominal one, and the solute is rejected into

375 the liquid phase. Therefore, a thin negative segregation layer forms at the bottom, while a liquid
 376 layer enriched with Pb is situated a few millimeters above. As solidification proceeds, these
 377 segregation phenomena become more pronounced.



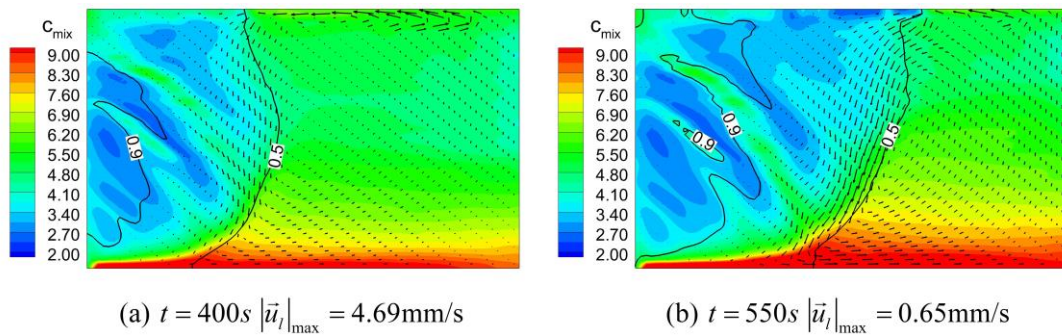
378
 379 Fig. 7—Various fields at different solidification times in case A: (a.1, b.1 and c.1) temperature and
 380 grain number density (n in m^{-3}), (a.2, b.2 and c.2) grain phase fraction (f_e) and velocity (\vec{u}_e), the
 381 black line shows the $f_e = 0.637$ level, (a.3, b.3 and c.3) averaged solute concentration (C_{mix} in
 382 wt. %Pb) and liquid phase velocity (\vec{u}_l), and (a.4, b.4 and c.4) solid phase fraction.

383 As described in section II-C, when the grain phase fraction f_e increases above the packing
384 fraction limit f_p^e , a packed region appears, which is shown below by the black line in Figure 7(a.2,
385 b.2 and c.2). At 10s, only a thin layer of packed grains is formed at the bottom. When grains arrive
386 at the right wall, they are dragged upwards by the liquid and tend to sediment at the same time,
387 thus resulting in their slight backwards flow followed by their dispersion in the bulk liquid. The
388 packed grain layer gradually piles up from the bottom of the cavity to the top. Some grains reach
389 the packing fraction limit before arriving at the right wall, which explains the formation of a gentle
390 slope towards the east (Figure 7(b.2 and c.2)). The upward liquid flow through the packed bed
391 depletes its solute concentration and enriches the liquid layer above the bed (Figure 7(a.3 and b.3)).
392 The downward liquid flow in the packed porous zone brings the solute down, forming a small
393 enriched pool at the bottom of the cavity (Figure 7(b.3)).

394 At 250 seconds of solidification, almost the entire cavity is occupied by packed grains, yet the
395 extradendritic liquid still circulates between them. Due to the large flow resistance in the packed
396 region, liquid flow in this area is weak, as shown in Figure 7(c.3), and maximum liquid flow
397 velocity in the packed region is only 6.5×10^{-4} m/s. However, this weak liquid flow can still
398 influence solute distribution if sufficient time is provided. As can be seen further in Figure 8, due
399 to buoyancy force and residual fluid flow, the enriched liquid descends and is replaced by the
400 liquid from upstream. Continued enrichment at the bottom leads to strong positive segregation
401 over the entire bottom. The overall result is that a region with semicircular shape forms near the
402 cooling face, corresponding to a negative segregated region at the same place, while positive
403 segregation forms in the bottom righthand region (Figure 7(c.3) and Figure 8).

404 Similar to the result from another equiaxed solidification model^[37,38] and the columnar
405 solidification model^[33,34,39], some segregation channels form near the cooling side. These channels
406 are determined by thermosolutal buoyancy and the local fluctuations in permeability of the packed
407 zone. Cells with higher solute content will have a lower liquidus temperature, and therefore, a
408 lower solid fraction for a given temperature. Therefore, envelope growth can be accelerated at one
409 location, or suppressed at another location depending on the flow field and solute concentration
410 distribution. Fluctuation of envelope growth will influence the permeability term in the
411 momentum equation, and then further affect the flow field. This mechanism generates a positive
412 feedback loop, allowing channels to continue to grow. In Figure 8, average solute concentration

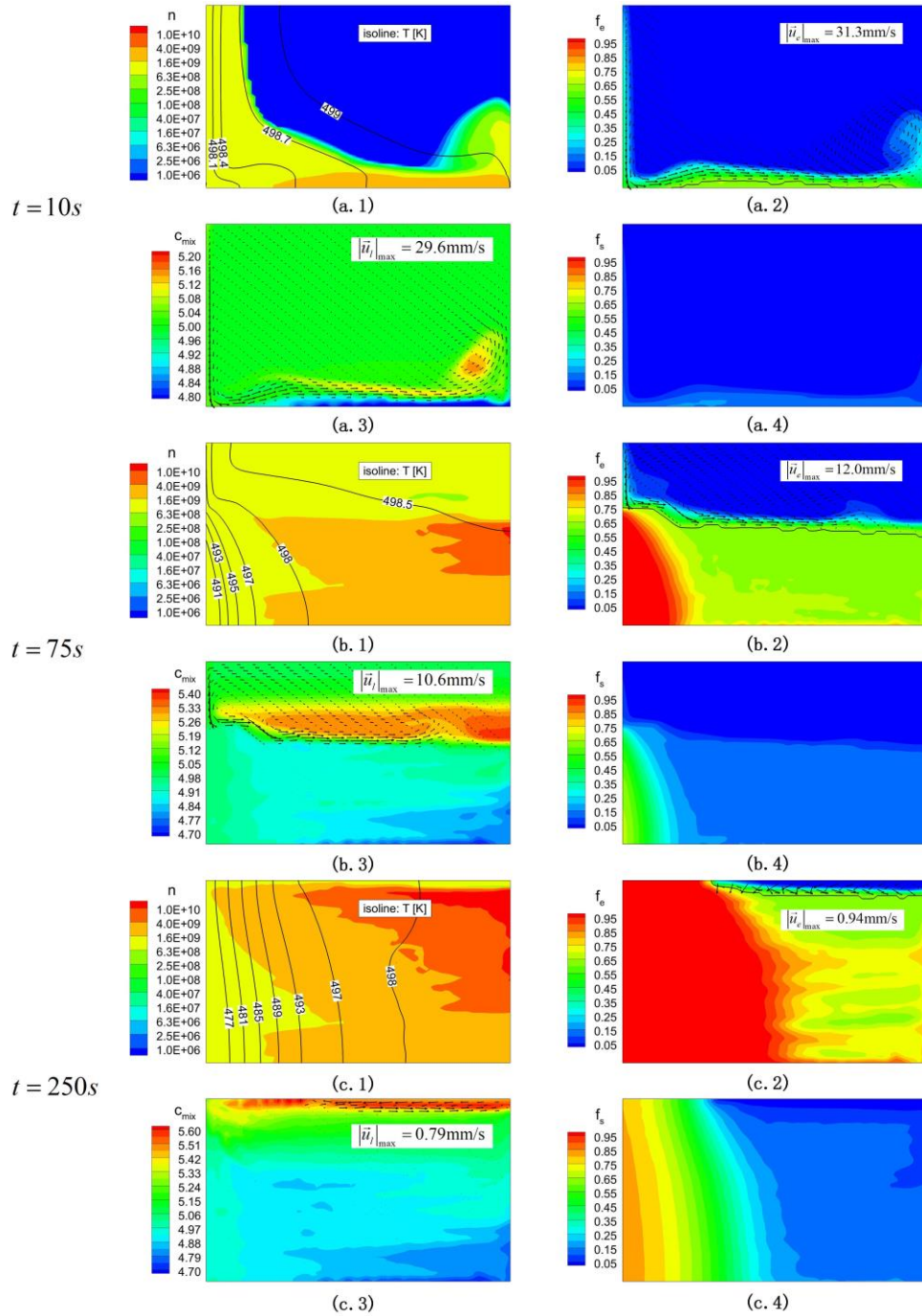
413 distribution is overlaid with the vectors for velocity in the extradendritic liquid and isolines of the
 414 solid fraction for $f_s = 0.5$ and $f_s = 0.9$. Areas with lower composition correspond to the
 415 protrusions of the solid into the bulk fluid flow during the earlier solidification stage. Liquid flow
 416 is most intense near the isline $f_s = 0.5$ from the lefthand side, i.e. in the zone $f_s > 0.5$. It is
 417 observed that a new channel appears on the existing channel from $t=400s$ to $t=550s$ (Figure 8).
 418 After that, channel formation stops but macrosegregation continue to evolve (compare Figure 8(b)
 419 and Figure 12).
 420



421 (a) $t = 400s$ $|\vec{u}_l|_{max} = 4.69mm/s$ (b) $t = 550s$ $|\vec{u}_l|_{max} = 0.65mm/s$
 422 Fig. 8—Evolution of macrosegregation with most grains being packed: solute distribution is
 423 shown with isolines of the solid fraction and vectors for flow velocity in l -phase (case A).

424
 425 **B. Results of case B**

426 Similar to case A, at the early stage of solidification of case B, the equiaxed grains appear and
 427 grow near the cooling side before sedimenting to the bottom, causing negative segregation (Figure
 428 9(a.3, b.3 and c.3)). The equiaxed grains pile up to form a packed region near the bottom.
 429 Diffusion length in case B always increases as envelope growth velocity decreases, meaning that
 430 the diffuse flux from the interdendritic liquid to the extradendritic liquid decreases with time and
 431 that bulk liquid enrichment is much less intense compared to the previous case. A weak
 432 enrichment leads to a higher constitutional undercooling, thus the envelope growth rate of grains
 433 remains high even when they get packed. Consequently, the extradendritic liquid between the
 434 grains rapidly disappears (Figure 9(b.2 and c.2)), and its convective velocity approaches zero
 435 (Figure 9(c.3) and Figure 10). A slightly enriched layer of the extradendritic liquid still remains on
 436 the top of packed grain region, because the buoyancy term related to solute concentration is small
 437 and the permeability of the packed grain region rapidly decreases. Although there is still
 438 interdendritic liquid inside the grain phase, the current model assumes that it has the velocity of



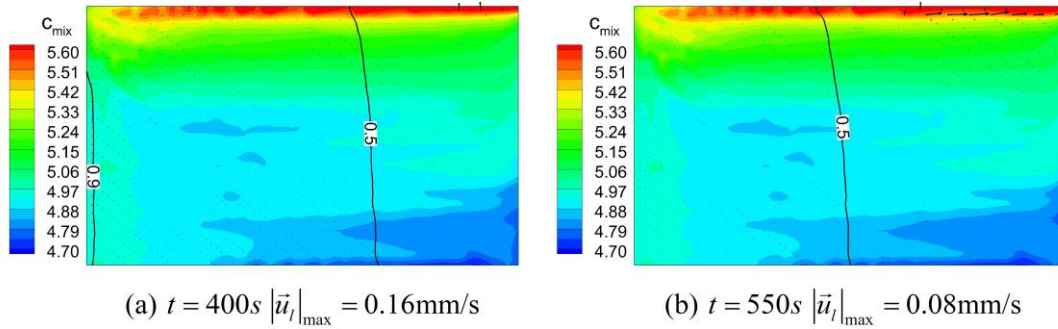
439

440 Fig. 9—Various fields at different solidification times in case B: (a.1, b.1 and c.1) temperature and
 441 grain number density (n in m^{-3}), (a.2, b.2 and c.2) grain phase fraction (f_e) and velocity (\vec{u}_e), the
 442 black line shows the $f_e = 0.637$ level, (a.3, b.3 and c.3) averaged solute concentration (C_{mix} in
 443 wt. %Pb) and liquid phase velocity (\vec{u}_l), and (a.4, b.4 and c.4) solid phase fraction.

444

445 the grain phase, yet, the latter is already packed, i.e. immovable. Therefore, after 250s, solute
 446 distribution barely changes, as can be seen in Figure 10. Although solidification proceeds in a

447 horizontal direction from the cooling side to the adiabatic side, slightly enriched liquid is then
 448 captured at the top by the packed grains whose fraction is not far from 1. Finally, an upward
 449 pointing concentration gradient forms in the sample (Figure 12(b)). For the same solidification
 450 case, a segregation pattern similar to that in case B was also obtained with a two-phase model.^[36]
 451



452
 453 Fig. 10—Evolution of macrosegregation with most grains being packed: solute distribution is
 454 shown with isolines of the solid fraction and vectors for flow velocity in l -phase (case B).

455

456 C. Effect of the diffusion length model on solidification results

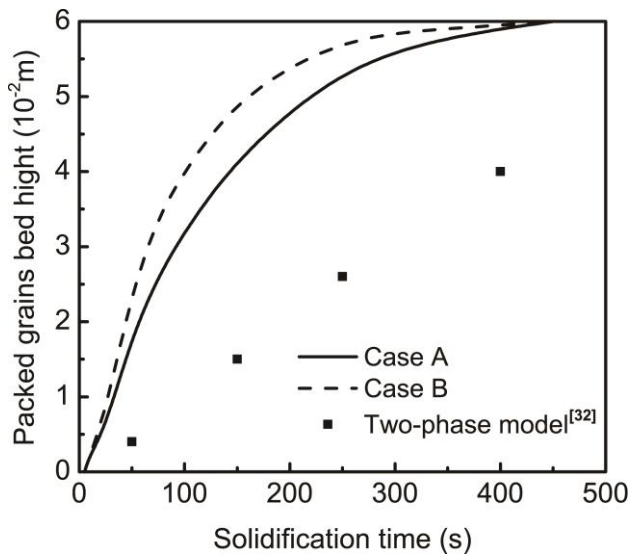
457 During the early stage of solidification, case B shows similar phenomena to case A, yet at 75 s,
 458 the two cases already present differences in grain growth and macrosegregation that become more
 459 pronounced with time.

460 A less intense enrichment of the extradendritic liquid and a higher grain growth velocity in case
 461 B lead to a faster increase in the height of the packed bed despite in this case a slower grain
 462 sedimentation velocity (compare Figures 7(b) and 8(b)). The packed bed grows fast at the
 463 beginning before slowing down due to the solidification process. In Figure 11, a height of the
 464 packed bed estimated from the results obtained by Založnik et al.^[36] with a two-phase model is
 465 also presented for comparison. The conclusion can be drawn that present three-phase models with
 466 the packing grain limit of 0.637 predict faster growth of the packed bed than the two-phase model
 467 with the packing limit of 0.3 for the solid fraction.

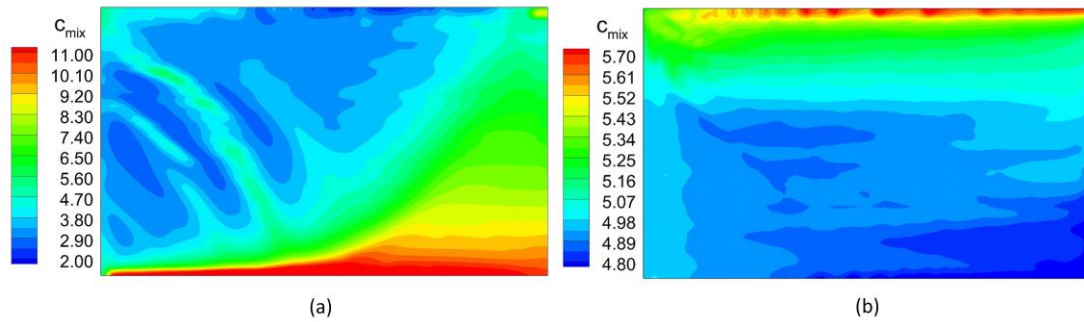
468 Regarding segregation, the formation of channels is observed in case A but not in case B.
 469 Similar to a columnar solidification,^[33,34,39] the channels are initiated near the cooling side and
 470 directed downwards following the fluid flow, which circumflexes the grains already packed at the
 471 lefthand wall, making the channels convex upward. For case B, the l -phase is quickly exhausted,
 472 meaning that the extradendritic liquid flow becomes too weak to affect solute distribution and to

473 form channels. A comparison of Figure 8 and Figure 10 shows that solid growth in case B is
 474 slower than in case A due to the faster diffusion of the solute from the solidifying dendrite to the
 475 extradendritic liquid. This is conversely to the zero-dimension solidification case which was
 476 considered in section II because the rejected solute is not conserved within a grain but is
 477 redistributed in the bulk liquid. Finally, in case A, positive enrichment forms at the bottom
 478 righthand part of the cavity, as shown in the macrosegregation map (Figure 12(a)), while in case B,
 479 a discontinuous positive segregation chain is presented at the top (Figure 12(b)). The segregation
 480 degree in case B is much smaller, from 4.8% to 5.8%, than that in case A, from 1.9% to 13.4%
 481 (Figure 12).

482 It should be noted that the segregation pattern in case A is close to the original experimental
 483 result (except channels),^[32] although mainly columnar grain structure was found in the experiment.
 484 This can be explained by the fact that in the present simulation, the dendrite equiaxed structure
 485 grows quickly before being packed into a bed that occupies the entire cavity. During further
 486 solidification, the packed grains cannot move anymore, and thus behave like a columnar dendrite
 487 structure.



488
 489 Fig. 11—Comparison of packed grain bed evolution.



490

491 Fig. 12—Segregation map for case A (a) and case B (b) at 1000s.

492 **V. Conclusions**

493 A modernized three-phase solidification model was proposed and applied for simulation of
 494 equiaxed dendritic solidification accounting for grain transport under the buoyancy flow. In the
 495 model, use of the Happel approximation for the momentum exchange coefficient between the two
 496 phases allows us to account for grain transport for the full grain fraction range. Furthermore, an
 497 additional criterion proposed for the treatment of the grain packing phenomenon allows us to take
 498 into account properly those grains whose fraction exceeds a theoretical packing limit but which
 499 were transported in the middle of the bulk liquid and, consequently, should not be blocked.
 500 However, the main novelty of the model is a new equation for calculation of diffusion length. The
 501 proposed diffusion length equation combines the factors affecting diffusion length in the
 502 extradendritic liquid, including a convective flow around the grains. The drastic effect of the
 503 adopted model is demonstrated with two simulations of the solidification of a binary alloy
 504 Sn-5wt%Pb. The only difference between them is in the calculation of diffusion length: case A
 505 uses a proposed equation, while case B uses a diffusion length purely dependent on envelope
 506 growth velocity. The numerical results show that the case including the proposed equation for
 507 diffusion length predicts a slower growth of the packed grain bed at the bottom of the cavity,
 508 formation of channels near the cooling side, and a final segregation pattern with an enriched layer
 509 at the bottom. The overall final segregation pattern is similar to the results obtained with the
 510 columnar model used earlier as well as with the experimental one.

511

512 **ACKNOWLEDGMENTS**

513 This work is a joint cooperation between the SIMAP laboratory of Grenoble INP (France) and
514 the Key Laboratory of EPM of Northeastern University (P. R. China). The authors gratefully
515 acknowledge financial support from the National Nature Science Foundation of China (Grant No.
516 U1760206), the National Key R&D Program of China (Grant No. 2017YFE0107900), the Project
517 of Introducing Talents of Discipline Innovation to Universities 2.0 (the 111 Project of China 2.0,
518 No. BP0719037) and China Scholarship Council (No. 201706080074). The SIMAP laboratory
519 acknowledges the financial support provided by the ESA-MAP MICAST project contract
520 14347/01/NL/SH.

521

522

NOMENCLATURE

c_i	solute concentration in i - phase (wt.%)	S_e^J	diffusion surface concentration of the grain phase (m^{-1})
c_{mix}	mix solute concentration (wt.%)	t	time (s)
c_{eut}	eutectic concentration (wt.%)	T	temperature (K)
c_l^*, c_s^*	equilibrium concentration at f - s or d - s interface (wt.%)	T_{eut}	eutectic temperature (K)
c_{env}	concentration at l - d interface (wt.%)	T_0	initial temperature (K)
c_p^i	specific heat for i -phase ($J\ kg^{-1}K^{-1}$)	ΔT	constitutional undercooling (K)
c_0	initial concentration (wt.%)	ΔT_{nucl}	nucleation temperature (K)
d_e, d_s	grain diameter (m)	\vec{u}_i	velocity vector of i - phase ($m\ s^{-1}$)
D_l	diffusion coefficient in liquid (m^2s^{-1})	\vec{U}_{ij}^D	momentum transfer rate from i - phase to j - phase ($kg\ m^{-2}s^{-2}$)
f_i	volume fraction of i - phase (1)	v_{env}	envelope growth velocity ($m\ s^{-1}$)
f_p^e, f_p^s	packing limit fraction (1)	v_{ds}	d - s interface growth velocity ($m\ s^{-1}$)
f_s^e	solid fraction within grains (1)	Greek Symbols	
\vec{F}_{Bi}	buoyancy force of i - phase ($kg\ m^{-2}s^{-2}$)	β_T	thermal expansion coefficient (K^{-1})
h_i	enthalpy of i - phase ($J\ kg^{-1}$)	β_c	solubility expansion coefficient (1)
H^*	interfacial heat transfer coefficient ($W\ m^{-3}K^{-1}$)	Φ_M	shape factor of dendritic envelope growth (1)
J_{ij}	species transfer rate from i - phase to j - phase ($m\ s^{-1}$)	Φ_J	sphericity of dendritic envelope (1)
k_i	thermal conductivity for i -phase ($W\ m^{-1}K^{-1}$)	Γ	gibbs thomson coefficient (m K)
k	solute partition coefficient (1)	λ_2	secondary arm spacing (m)
K_{ij}	liquid-equiaxed drag coefficient ($kg\ m^{-3}s^{-1}$)	μ_i	viscosity of i - phase ($kg\ m^{-1}s^{-1}$)
l_i	diffusion length of i - phase (m)	ρ_i	density of i - phase ($kg\ m^{-3}$)
L	latent heat ($J\ kg^{-1}$)	ρ_{ref}	reference density ($kg\ m^{-3}$)
m	slope of liquidus in phase diagram (K)	ρ_s^b	density of solid phase for buoyancy
M_Φ	mass transfer rate from nucleation ($kg\ m^{-3}s^{-1}$)	Ψ_i	a intensive medium property (-)
M_{ij}	mass transfer rate from i - phase to j - phase ($kg\ m^{-3}s^{-1}$)	Subscripts	
n_{max}	maximum equiaxed grain density (m^{-3})	d	interdendritic liquid phase

n	grain number density (m^{-3})	$e: d+s$	exquiaxed grain phase
N_{Φ}	nuclei production rate ($\text{m}^{-3}\text{s}^{-1}$)	$f: l+d$	liquid phase
Re	Reynolds number (1)	l	extradendritic liquid phase
Sh	Sherwood number (1)	s	interdendritic solid phase
S_e^M	surface concentration of the equivalent sphere (m^{-1})		

523 *Note:*

524 The symbols related to averaging procedures are omitted in the paper, i.e. a field property

525 averaged over its proper phase $\langle \Psi_i \rangle^i$ is replaced with Ψ_i for simplicity.

526 **REFERENCES:**

- 527 1 M. Wu, L. Könözsy, A. Ludwig, W. Schützenhöfer, and R. Tanzer: *Steel Res. Int.*, 2008, vol. 79, pp. 637–
528 44.
- 529 2 M. Wu, A. Ludwig, and A. Kharicha: *Metals (Basel)*, 2019, vol. 9, p. 229.
- 530 3 P. Thévoz, J.L. Desbiolles, and M. Rappaz: *Metall. Trans. A*, 1989, vol. 20, pp. 311–22.
- 531 4 N. Leriche, H. Combeau, C.A. Gandin, and M. Založnik: *IOP Conf. Ser. Mater. Sci. Eng.*, 2015, vol. 84,
532 pp. 1–8.
- 533 5 A.I. Ciobanas and Y. Fautrelle: *J. Phys. D. Appl. Phys.*, 2007, vol. 40, pp. 3733–62.
- 534 6 A.I. Ciobanas and Y. Fautrelle: *J. Phys. D. Appl. Phys.*, 2007, vol. 40, p. 4310.
- 535 7 C.Y. Wang and C. Beckermann: *Metall. Mater. Trans. A*, 1993, vol. 24, pp. 2787–802.
- 536 8 Y. Zheng, M. Wu, E. Karimi-Sibaki, A. Kharicha, and A. Ludwig: *Int. J. Heat Mass Transf.*, 2018, vol.
537 122, pp. 939–53.
- 538 9 R. Ananth and W.N. Gill: *J. Cryst. Growth*, 1988, vol. 91, pp. 587–98.
- 539 10 D. V. Alexandrov and P.K. Galenko: *Uspekhi Fiz. Nauk*, 2014, vol. 184, pp. 833–50.
- 540 11 J. Lipton, M.E. Glicksman, and W. Kurz: *Mater. Sci. Eng.*, 1984, vol. 65, pp. 57–63.
- 541 12 B. Appolaire, H. Combeau, and G. Lesoult: *Mater. Sci. Eng. A*, 2008, vol. 487, pp. 33–45.
- 542 13 C.Y. Wang and C. Beckermann: *Metall. Mater. Trans. A*, 1996, vol. 27, pp. 2754–64.
- 543 14 M. Rappaz and P.H. Thévoz: *Acta Metall.*, 1987, vol. 35, pp. 2929–33.
- 544 15 M. Wu, A. Ludwig, A. Bührig-Polaczek, M. Fehlbier, and P.R. Sahm: *Int. J. Heat Mass Transf.*, 2003, vol.
545 46, pp. 2819–32.
- 546 16 M. Založnik and H. Combeau: *Comput. Mater. Sci.*, 2010, vol. 48, pp. 1–10.
- 547 17 J. Ni and C. Beckermann: *J. Mater. Process. Manuf. Sci.*, 1993, vol. 2, pp. 217–31.
- 548 18 J. Ni and C. Beckermann: *Metall. Trans. B*, 1991, vol. 22, pp. 349–61.
- 549 19 A. Badillo, D. Ceynar, and C. Beckermann: *J. Cryst. Growth*, 2007, vol. 309, pp. 216–24.
- 550 20 R.B. Bird, W.E. Stewart, and E.N. Lightfoot: *Transport Phenomena John Wiley and Sons*, NY, 1960.
- 551 21 A. Ludwig and M. Wu: *Metall. Mater. Trans. A*, 2002, vol. 33, pp. 3673–83.
- 552 22 M. Wu and A. Ludwig: *Acta Mater.*, 2009, vol. 57, pp. 5632–44.
- 553 23 J. Happel: *AIChE J.*, 1958, vol. 4, pp. 197–201.
- 554 24 A. Plotkowski and M.J.M. Krane: *Appl. Math. Model.*, 2016, vol. 40, pp. 9212–27.
- 555 25 D. Jiang and M. Zhu: *Metall. Mater. Trans. B*, 2016, vol. 47, pp. 3446–58.
- 556 26 M.A. Martorano and V.B. Biscuola: *Model. Simul. Mater. Sci. Eng.*, 2006, vol. 14, pp. 1225–43.
- 557 27 M. Torabi Rad, M. Založnik, H. Combeau, and C. Beckermann: *Materialia*, 2019, vol. 5, p. 100231.
- 558 28 D. Jiang and M. Zhu: *Metall. Mater. Trans. B*, 2017, vol. 48, pp. 444–55.
- 559 29 M.J.M. Krane: *Appl. Math. Model.*, 2004, vol. 28, pp. 95–107.
- 560 30 A. Olmedilla, M. Založnik, T. Messmer, B. Rouat, and H. Combeau: *Phys. Rev. E*, 2019, vol. 99, p.
561 12907.
- 562 31 A. Olmedilla, M. Založnik, B. Rouat, and H. Combeau: *Phys. Rev. E*, 2018, vol. 97, p. 012910.
- 563 32 D.J. Hebditch and J.D. Hunt: *Met. Trans*, 1974, vol. 5, pp. 1557–64.
- 564 33 N. Ahmad, J. Rappaz, J.-L. Desbiolles, T. Jalanti, M. Rappaz, H. Combeau, G. Lesoult, and C. Stomp:
565 *Metall. Mater. Trans. A*, 1998, vol. 29, pp. 617–30.
- 566 34 A. Kumar, B. Dussoubs, M. Založnik, and H. Combeau: *J. Phys. D. Appl. Phys.*, 2009, vol. 42, p. 105503.
- 567 35 T.-T.-M. Nguyen, C.-A. Gandin, H. Combeau, M. Založnik, and M. Bellet: *Metall. Mater. Trans. A*, 2018,
568 vol. 49, pp. 1725–48.
- 569 36 M. Založnik, A. Kumar, and H. Combeau: *Comput. Mater. Sci.*, 2010, vol. 48, pp. 11–21.

570 37 A. Plotkowski and M.J.M. Krane: *Comput. Mater. Sci.*, 2016, vol. 124, pp. 238–48.
571 38 A. Plotkowski and M.J.M. Krane: *Int. J. Heat Mass Transf.*, 2016, 100, vol. 100.
572 39 R. Boussaa, L. Hachani, O. Budenkova, V. Botton, D. Henry, K. Zaidat, H. Ben Hadid, and Y. Fautrelle:
573 *Int. J. Heat Mass Transf.*, 2016, vol. 100, pp. 680–90.
574 40 T. Carozzani, C.-A. Gandin, H. Dignonnet, M. Bellet, K. Zaidat, and Y. Fautrelle: *Metall. Mater. Trans. A*,
575 2013, vol. 44, pp. 873–87.
576
577

578 **Caption list**

579 **Fig.1.** (a) Schematic representation of grain growth with phase assignment, and (b)effect of
580 diffusion length on average solute concentration in each phase.

581 **Table I.** Diffusion length ahead of the dendrite tip in equiaxed solidification models

582 **Fig.2.** Schematic figure for different unions of phases: (a) solid dendrite (s- phase) and liquid
583 phase (f-phase), (b) equiaxed grain phase (e-phase) and extradendritic liquid phase (l-
584 phase), and (c) the solid dendrite (s-phase), inter- and extradendritic liquid phases (d- and
585 l-phases).

586 **Table II.** Coefficient in the equation for the momentum exchange, Eq. [2].

587 **Table III.** Conservation equations, source terms, and auxiliary expressions.

588 **Fig.3.** Solidification in a zero dimension uniformly solidifying system obtained with different
589 models (Eqs. [35] through [38]) for diffusion length l_t : (a) variation of diffusion length l_t
590 in time, (b) evolution of the solid and grain fractions and (c) temperature evolution.

591 **Fig. 4.** Comparison of (a) dimensionless momentum exchange coefficient between l- and e-
592 phases and (b) settling velocity between different models.

593 **Fig. 5.** Scheme algorithm scheme.

594 **Fig. 6.** Illustration for the solidification problem under consideration.

595 **Table IV.** Phase diagram data and Material properties.

596 **Fig. 7.** Various fields at different solidification times in case A: (a.1, b.1 and c.1) temperature and
597 grain number density (n in m^{-3}), (a.2, b.2 and c.2) grain phase fraction (f_e) and velocity
598 (\vec{u}_e), the black line shows the $f_e = 0.637$ level, (a.3, b.3 and c.3) averaged solute
599 concentration (c_{mix} in wt. %Pb) and liquid phase velocity (\vec{u}_l), and (a.4, b.4 and c.4) solid
600 phase fraction.

601 **Fig. 8.** Evolution of macrosegregation with most grains being packed: solute distribution is shown
602 with isolines of the solid fraction and vectors for flow velocity in l-phase (case A).

603 **Fig.9.** Various fields at different solidification times in case B: (a.1, b.1 and c.1) temperature and
604 grain number density (n in m^{-3}), (a.2, b.2 and c.2) grain phase fraction (f_e) and velocity (\vec{u}_e), the
605 black line shows the $f_e = 0.637$ level, (a.3, b.3 and c.3) averaged solute concentration (c_{mix} in
606 wt. %Pb) and liquid phase velocity (\vec{u}_l), and (a.4, b.4 and c.4) solid phase fraction.

607 **Fig. 10.** Evolution of macrosegregation with most grains being packed: solute distribution is
608 shown with isolines of the solid fraction and vectors for flow velocity in l-phase (case B).

609 **Fig. 11.** Comparison of the packed grains bed evolution.

610 **Fig. 12.** Segregation map for case A (a) and case B (b) at 1000s.

611

Table I. Diffusion length ahead of the dendrite tip in equiaxed solidification models

Reference	Phases type of grain	Diffusion length l_l or l_f
Rappaz and Thevoz [14]	<i>l, d, s</i> <i>dendritic</i>	$l_l = \frac{D_l}{v_{tip}}$ (No flow)
Ni and Beckermann ^[17]	<i>f, s</i> <i>globular</i>	$l_f = \frac{d_s}{2} \left(\frac{1}{1 - (1 - f_f)^{\frac{1}{3}}} + \frac{Sc^{\frac{1}{3}} Re^a}{3f_f} \right)^{-1}$
Wang and Beckermann ^[13]	<i>l, d, s</i> <i>dendritic</i>	$l_l = \frac{d_e}{2 + 0.865 \left(\frac{C_\epsilon}{f_l} \right)^{1/3} \left(\frac{f_l \bar{u}_l - \bar{u}_e }{D_l} \right)^{1/3}}$ with $C_\epsilon = C_\epsilon(f_l)$
Appolaire and Combeau ^[12]	<i>l, d, s</i> <i>dendritic (single crystal in infinite medium)</i>	$l_l = \min \left(\frac{d_e}{Sh}, \frac{D_l}{v_{tip}} \right)$ where $Sh = 2 + 0.6Sc^{1/3} Re^{1/2}$
Wu and Ludwig ^[22]	<i>l, d, s</i> <i>dendritic</i>	$l_l = \begin{cases} \frac{d_e}{2} & \text{globular growth} \\ \frac{D_l}{v_{env}} & \text{dendritic growth} \end{cases}$

615 **Table II. Coefficient in the equation for the momentum exchange, Eq. [2]**

Reference	Phases, union of phases, type of grain	Coefficients for Eq. [2]
Wu and Ludwig ^[22]	<i>l, e = (d ∪ s)</i> <i>dendritic</i>	$K_{le} = F_k(f_l, d_e) \frac{\mu_l}{K} = \begin{cases} \frac{180\mu_l f_e^2}{f_l d_e^2} & f_e < f_{sc} \\ \frac{\mu_l f_l^2}{K} & f_e > f_{sc} \end{cases}$ $F_{CD} = \frac{3 f_s}{4 d_s}, \quad C_D = \frac{48C_{ke}(1-f_f)}{Re} + C_{ie}$
Ni and Beckermann ^[17]	<i>f, s</i> <i>globular</i>	$Re = \frac{\rho f_f d_s}{\mu_f} \vec{u}_f - \vec{u}_s $ $C_{ke} = 0.5 \text{ and } C_{ie} = 7/3 \text{ for } f_f \leq 0.5$ $C_{ke}(f_f, Re), C_{ie}(f_f, Re) \text{ for } f_f > 0.5$
Wang and Beckermann ^[13]	<i>l, d, s</i> <i>dendritic</i>	$K_{fs} = 4f_f^2 \beta^2 \frac{\mu_l}{d_e^2} \quad \text{where}$ $\beta = \frac{\beta_d}{[(1-f_l)^n + (\beta_d/\beta_l)^{2n}]^{1/2n}}$
Apollaire and Combeau ^[12]	<i>l, d, s</i> <i>dendritic</i> <i>(single crystal in infinite medium)</i>	$F_{CD} = \frac{\rho_f \pi d^2 \Omega}{8}, \quad C_D = \frac{c'_D}{1.2376 \log(\Phi/0.1556)} \quad \text{where}$ $C'_D(Re), \Omega\left(\frac{d}{\sqrt{K}}\right), \Phi \text{ sphericity, } K \text{ from Kozeny-Carman}$ $\text{Slurry region: } F_{CD} = \frac{3\rho f_e}{4 d_e} \quad C_D = \frac{48C_{ke}(1-f_l)}{Re} + C_{ie}$
Leriché and Combeau ^[4]	<i>f = (l ∪ d), s</i> <i>dendritic</i>	$C_{ke} = 0.5 \text{ and } C_{ie} = 7/3 \text{ for } f_e > 0.5$ $C_{ke}(f_l, Re), C_{ie}(f_l, Re) \text{ for } f_e \leq 0.5$ $\text{Packed region: } K = \frac{\lambda_2^2}{20\pi^2} \frac{f_f^3}{(1-f_f)^2}$

616 **Table III. Conservation equations, source terms, and auxiliary expressions**

1. Conservation equations			
Mass	$\frac{\partial(f_l \rho_l)}{\partial t} + \nabla(f_l \rho_l \bar{u}_l) = M_{el} - M_\Phi$	[3]	
	$\frac{\partial(f_e \rho_e)}{\partial t} + \nabla(f_e \rho_e \bar{u}_e) = M_{ie} + M_\Phi$	[4]	
	$\frac{\partial(f_e f_s^e \rho_s)}{\partial t} + \nabla(f_e f_s^e \rho_s \bar{u}_e) = M_{ds} + M_\Phi$	[5]	
Momentum	$\frac{\partial(f_l \rho_l \bar{u}_l)}{\partial t} + \nabla(f_l \rho_l \bar{u}_l \bar{u}_l) = -f_l \nabla p + \nabla[\mu_l f_l (\nabla \bar{u}_l + (\nabla \bar{u}_l)^T)] + \bar{u}_l M_{el} + \bar{F}_{Bl} + \bar{U}_{el}^D$	[6]	
	$\frac{\partial(f_e \rho_e \bar{u}_e)}{\partial t} + \nabla(f_e \rho_e \bar{u}_e \bar{u}_e) = -f_e \nabla p + \nabla[\mu_e f_e (\nabla \bar{u}_e + (\nabla \bar{u}_e)^T)] + \bar{u}_e M_{ie} + \bar{F}_{Be} + \bar{U}_{ie}^D$	[7]	
Energy	$\frac{\partial(f_l \rho_l h_l)}{\partial t} + \nabla(f_l \rho_l \bar{u}_l h_l) = \nabla(k_l f_l \nabla T) + LM_{ds} f_l + M_{el} h_l + Q_{el}$	[8]	
	$\frac{\partial(f_e \rho_e h_e)}{\partial t} + \nabla(f_e \rho_e \bar{u}_e h_e) = \nabla(k_e f_e \nabla T) + LM_{ds} f_e + M_{ie} h_l + Q_{ie}$	[9]	
	where $h_l = \int_{T_{ref}}^{T_l} c_p^l dT + h_l^{ref}$, $h_e = \int_{T_{ref}}^{T_e} c_p^e dT + h_e^{ref}$		
Solute	$\frac{\partial(f_l \rho_l c_l)}{\partial t} + \nabla(f_l \rho_l \bar{u}_l c_l) = \nabla(D_l f_l \nabla c_l) + J_e$	[10]	
	$\frac{\partial(f_e \rho_e c_e)}{\partial t} + \nabla(f_e \rho_e \bar{u}_e c_e) = J_{ie}$	[11]	
	$\frac{\partial(f_s \rho_s c_s)}{\partial t} + \nabla(f_s \rho_s \bar{u}_e c_s) = J_{ds}$	[12]	
Grain number density	$\frac{\partial}{\partial t} n + \nabla(\bar{u}_e n) = N_\Phi$	[13]	
2. Source terms			
Mass	$M_{ie} = -M_{el} = \rho_l \cdot S_e^M \cdot v_{env}$	[14]	
	$M_{ds} = f_e \cdot \rho_s \cdot \frac{2 \cdot f_d^e}{\lambda_2} \cdot v_{ds}$	[15]	
	$M_\Phi = N_\Phi \rho_l \cdot \frac{1}{6} \pi d_0^3$	[16]	
Momentum	$\bar{F}_{Bl} = f_l \rho_l \bar{g} [\beta_T (T_{ref} - T_l) + \beta_c (c_{ref} - c_l)]$	[17]	
	$\bar{F}_{Be} = f_d \rho_d \bar{g} [\beta_T (T_{ref} - T_e) + \beta_c (c_{ref} - c_d)] + f_s (\rho_s^b - \rho_{ref}) \bar{g}$	[18]	
	$\bar{U}_{ie}^D = -\bar{U}_{el}^D = K_{ie} (\bar{u}_l - \bar{u}_e) = 4 f_l^2 \beta^2 \frac{\mu_l}{d_e^2} (\bar{u}_l - \bar{u}_e)$	[19]	
Energy	$Q_{ie} = -Q_{el} = H^* (T_l - T_e)$	[20]	
	where $H^* = 1 \times 10^9 \text{ W m}^{-3} \text{ K}^{-1}$ (infinite)		
Solute	$J_{ie} = -J_{el} = -\rho_l \cdot S_e^J \cdot \frac{D_l \cdot (\bar{c}_{env} - c_l)}{l_l} + M_{ie} \cdot \bar{c}_{env} + M_\Phi \cdot c_s^*$	[21]	
	$J_{ds} = c_s^* \cdot (M_{ds} + M_\Phi)$	[22]	
Grain number density	$N_\Phi = \begin{cases} f_l (n_{max} - n) / \Delta t, & \Delta T > \Delta T_{nucl} \text{ or } n < 1 \\ 0, & \text{else} \end{cases}$	[23]	
3. Auxiliary expressions			
$c_l^* = \frac{T_l - T_0}{m}$	[24]	$\bar{c}_{env} = \frac{l_d c_l + l_l c_d}{l_d + l_l}$	[25]
$c_s^* = k \cdot c_l^*$	[26]	$c_{mix} = \frac{f_l \rho_l c_l + f_e \rho_e c_e}{f_l \rho_l + f_e \rho_e}$	[27]
$c_d = \frac{f_e \cdot c_e - f_s \cdot c_s}{f_d}$	[28]	$S_e^M = f_l \cdot (36\pi \cdot n)^{1/3} \cdot f_e^{2/3}$	[29]
$S_e^J = (36\pi \cdot n)^{1/3} \cdot f_e^{2/3} / \Phi_J$	[30]	$l_d = \frac{f_d \lambda_2}{2 f_e}$	[31]
l_l see Eq. [35]		$\beta = \left\{ \frac{9}{2} f_e \frac{2 + \frac{4}{3} f_e^{\frac{5}{3}}}{2 - 3 f_e^{\frac{1}{3}} + 3 f_e^{\frac{5}{3}} - 2 f_e^2} \right\}^{1/2}$	[32]
$v_{env} = \Phi_M \frac{D_l \cdot m_l \cdot (\kappa - 1) \cdot c_l^*}{\pi^2 \cdot \Gamma} \cdot \left[\frac{(c_l^* - c_l)}{c_l^* (1 - k)} \right]^2$	[33]	$v_{ds} = \frac{D_l}{l_d} \cdot \frac{c_l^* - c_d}{c_l^* - c_s^*}$	[34]

619 **Table IV. Phase diagram data and Material properties**

	Symbol	Units	Value	Ref.
<i>Phase diagram</i>				
Melting temperature of pure Sn	T_{Sn}	K	505.15	
Eutectic temperature	T_{eut}	K	456.15	
Partition coefficient	k	1	0.0656	[36]
Initial solute concentration(Pb)	c_0	wt. %	5.0	
Liquidus slope	m	K	-128.6	[36]
<i>Material properties</i>				
Reference mass density	ρ_{ref}	kg m ⁻³	7000	[36]
Density of solid for buoyancy force	ρ_s^b	kg m ⁻³	7143	[36]
Reference temperature for density	T_{ref}	K	499.15	
Liquid solutal expansion coefficient	β_c	wt. % ⁻¹	5.3×10 ⁻³	[36]
Liquid thermal expansion coefficient	β_T	K ⁻¹	6.0×10 ⁻⁵	[36]
Reference solute concentration for density	c_{ref}	wt. %	5.0	
Specific heat	c_p^l, c_p^e	J kg ⁻¹ K ⁻¹	260	[36]
Thermal conductivity	k_l, k_e	W m ⁻¹ K ⁻¹	55	[36]
Latent heat	L	J kg ⁻¹	61000	[36]
Diffusion coefficient for liquid	D_l	m ² s ⁻¹	1×10 ⁻⁸	[36]
Dynamic viscosity	μ_l, μ_e	kg m ⁻¹ s ⁻¹	0.001	[36]
Volume heat transfer coefficient	H^*	W m ⁻³ K ⁻¹	1×10 ⁹	[21]
Gibbs –Thomson coefficient	Γ	m K	2×10 ⁻⁷	[40]
Maximum grain number density	n_{max}	m ⁻³	1×10 ⁹	[36]
Initial grain diameter	d_0	m	1×10 ⁻⁶	
Secondary arm spacing	λ_2	m	9×10 ⁻⁵	
Shape factor for dendrite growth	Φ_M	1	0.683	[22]
Sphericity	Φ_J	1	0.283	[22]
Packing limit fraction	f_p^e	1	0.637	[22]